Article

Effect of nitrogen ion implantation on the cavitation erosistance and cobalt-based solid solution phase transformations of HIPed Stellite 6

Mirosław Szala [1,*], Dariusz Chocyk [1], Anna Skic [2], Mariusz Kamiński [1], Wojciech Macek [3] and Marcin Turek [4]

[1] Faculty of Mechanical Engineering, Lublin University of Technology, Nadbystrzycka 36D, 20-618 Lublin, Poland; m.szala@pollub.pl (M.S.); <u>d.chocyk@pollub.pl</u> (D.C.); <u>mariusz.kaminski@pollub.pl</u> (M.K.)

[2] Department of Mechanical Engineering and Automatic Control, University of Life Sciences, Głęboka 28, 20-612 Lublin, Poland; anna.skic@up.lublin.pl

[3] Opole University of Technology, Prószkowska 76, 45-758 Opole, Poland (W.M); wojciech.macek@yahoo.com

[4] Institute of Physics, Maria Curie Sklodowska University in Lublin, M. Curie-Sklodowska sq 1, 20-031 Lublin, Poland; mturek@kft.umcs.lublin.pl

* Correspondence: m.szala@pollub.pl (M.S.)

Abstract: From the wide range of engineering materials traditional Stellite 6 alloy exhibits excellent cavitation erosion (CE) resistance. In this work, the effect of nitrogen ion implantation of HIPed Stellite 6 on the improvement of CE resistance and both cobalt-rich matrix phase transformation due to nitrogen implantation and CE were stated. The CE resistance of stellites ion-implanted by 120 keV N^+ ions two fluences: 5×10^{16} cm^{-2} and 1×10^{17} cm^{-2} were comparatively analysed with the unimplanted stellite and AISI 304 stainless steel. CE tests were conducted according to ASTM G32 with stationary specimen method. Erosion rate curves and mean depth of erosion confirm that the nitrogen implanted HIPed Stellite 6 two times exceeds the resistance to CE than unimplanted stellite, and has almost 10 times higher CE reference than stainless steel. The X-ray diffraction (XRD) confirms that HIPed Stellite 6 nitrogen ion implantation favours transformation of the ε(hcp) to γ(fcc) structure. Unimplanted stellite ε-rich matirx is less prone to plastic deformation than γ and consequently, increase of γ phase effectively holds carbides in cobalt matrix and prevents Cr_7C_3 debonding. This phenomenon elongates three times the CE incubation stage, slows erosion rate and mitigates the material loss. Metastable γ structure formed by ion implantation consumes the cavitation load for work-hardening and γ → ε martensitic transformation. In further CE stages, phases transform as for unimplanted alloy namely, the cavitation-inducted recovery process, removal of strain, dislocations resulting in increase of γ phase. The CE mechanism was investigated using a surface profilometer, atomic force microscopy, SEM-EDS and XRD. HIPed Stellite 6 wear behaviour relies on the plastic deformation of cobalt matrix, starting at Cr_7C_3/matrix interfaces. Once the Cr_7C_3 losing their restrain, are debonding and removed. Carbides detachment creates cavitation pits which initiate cracks propagation through cobalt matrix, the loss of matrix phase and CE proceeds with a detachment of massive chunk of materials.

Keywords: cavitation erosion, ion implantation, wear, failure analysis, cobalt alloy, stellite 6, damage mechanism, phase transformation.

1. Introduction

Cobalt-based alloys with additions of Cr, C, W, and/or Mo, named as Stellites, present superior performance in various environments such as corrosive, high temperature, wear and erosion conditions. They can well behave in advanced engineering applications such as the primary circuit in nuclear pressurized water reactors [1], engine components [2], oil and gas applications [3], elevated temperature metal forming tools [4]. Stellites components are fabricated with various techniques, more often by overlay welding [5,6],

casting [7,8] or using surface techniques likewise HVOF [9], cold spray [10], laser cladding [11], laser remelting [12] or conventional machining [13]. The functional properties of stellites depend on the fabrication process. One of the most widespread cobalt based alloy is Stellite 6 and component made of this alloy are manufactured not only by casting and welding, thermal deposition methods but also by powder metallurgy, namely Hot Isostatically Pressing (HIP) [3,14–16]. Cobalt based materials are among the most cavitation erosion-resistant materials commercially available and chemical composition of Stellite 6 alloy exhibits excellent cavitation erosion (CE) resistance. Therefore, Stellite 6 superior CE behaviour is documented by many scientific papers, for the stellites produced as alloy weld overlays [17], plasma transferred arc (PTA) overlay welding [18], laser cladding [11], shielded metal arc welding (SMAW) [19] and also HVOF deposited Stellite 6 coatings [20] and cobalt-based WC-Co cermet's deposits [21–23]. Unfortunately, as far as the authors' knowledge no paper describes cavitation properties of the powder metallurgy satellites and analysis its cavitation wear behaviour of HIPed Stellite 6.

Besides, there is a systematic demand to improve its operation-time of stellites by employing various post-treatment techniques presented by the literature. Thus, stellite laser remelting [24], alloying [25] or ion implantation [26] are employed to modify the properties of Co-based alloy surface layer. Even so, these processes are mostly applied for increasing stellites tribological, corrosion or erosion resistance, it should be emphasized that limited papers focus on the effect of stellites treatment on their CE resistance. Especially, ion implantation is one of the most promising anti-wear processes, which has a positive effect in the range of engineering applications such as corrosive [27] and sliding wear [26,28] performance of different metallic surfaces. Moreover, the investigation into the anti-cavitation application of different ion types and fluences into the metallic materials were discussed by the literature. It is confirmed that the ion implantation of stainless steel grade 13Cr4Ni dosed with nitrogen [29], mild carbon steel with nitrogen and titanium [30], titanium implanted cobalt-based carbide [31] results in increasing CE resistance.

The Stellite alloys microstructure consists of Co-based solid solution and second phases. Cobalt matrix is usually formed by the different fraction of hexagonal close-packed (hcp) to face-centered cubic (fcc) phases, and these structures can transform under the action of temperature, strain, cobalt alloy processing, treatment, strain affected operation conditions ect. [12,32,33]. Although The cobalt structure undergoes a phase transition from the high temperature fcc structure, stabile above approx. 700 K, to the low temperature hcp phase being thermodynamically stable at room temperature, both structures are usually present. Moreover, cobalt fcc → hcp transformation is currently designated as martensitic due to its diffusionless character, its considerable thermal hysteresis and the typical nucleation and growth processes [34]. On the other hand, reverse transformation kinetics, namely the hcp → fcc phase transformation mechanism in cobalt, is still not fully explained by the literature [32,35,36]. Similarly, along with the literature survey, neither the cobalt-based solid solution phase transformation due to nitrogen ion implantation nor the effect of the CE on cobalt-matrix phase transformation of implanted has been investigated. Moreover, according to the authors knowledge, no attention has been paid by the scientific literature to the nitrogen ion implantation effect on the CE of HIPed Stellite 6.

Therefore, this work aims to investigate the ion implantation effect on the cavitation erosion resistance of HIPed Stellite 6 cobalt alloy. Also, the effect of nitrogen dose was taken into account during the analysis of cavitation erosion mechanism of HIPed stellite 6 the cavitation inducted cobalt-based solid solution phase transformation induced was preliminarily discussed.

2. Materials and Methods

2.1. Samples preparation, ion-implantation and materials characterization

The samples were machined from a round bar made of HIP-consolidated (Hot Isostatically Pressed) cobalt alloy grade Stellite 6 with diameter of 25 mm and 10 mm height.

Then the flat test surface was mirror-polished to obtain the Sa<0.06 μm and Sz<0.8 μm, and subsequently treated with nitrogen ion implantation. Implantation was performed using ion implantation UNIMAS at Institute of Physics of Maria Curie-Skłodowska University in Lublin (Poland) equipped with arc discharge plasma ion described in [37], in configuration without any internal evaporator. Irradiations were done with 120 keV N^+ ions with fluences 5×10^{16} N^+/cm^{-2} (marked as K1 sample) and 1×10^{17} N^+/cm^{-2} (marked as K2 sample) and unimplanted sample is named as K0. The distribution of implanted nitrogen ions and radiation damage (vacancies) caused by the implantation over the sample depth calculated using the SRIM software [38] based on the alloy chemical composition. The chemical composition of the tested alloy, given in Table 1, and measured Vickers hardness 507±22 HV0.2 corresponds to literature data of Stellite 6 alloys [3,39,40].

Table 1. The chemical compositions of HIPed Stellite 6.

Chemical composition of HIPed Stellite 6, wt%								
Co	Cr	W	C	Fe	Ni	Si	Mn	Mo
bal.	28.40	6.15	1.34	2.00	2.18	0.60	0.45	1.45

*Measured using XRF.

To investigate the microstructure of implanted and unimplanted samples the SEM-EDS and XRD methods were employed. The X-ray diffraction (XRD) measurements were made using the high-resolution X-ray diffractometer (Empyrean Panalytical, The Netherlands). CuKα (λ_{Cu} = 1.5418 Å) radiation was used and measurements were performed in the θ-2θ geometry over a range from 30° to 100° with step size of 0.01° and counting time 6 s per data point. The crystalline phase in the samples was identified using High Score Plus software package. The diffraction profiles were comparatively analysed.

2.2. Cavitation testing and damage evaluation

Cavitation erosion tests were prepared using a vibratory test rig and test conditions described in previous papers [41,42]. Cavitation was generated by a magnetostrictive-driven apparatus, resonating at 20 kHz with a peak-to-peak displacement amplitude of 50 μm. The stainless steel AISI 304 was used as a reference sample. In the current work, the standoff between the sonotrode-tip and the specimen surface was set equal to $1^{-0.05}$ mm. The apparatus conformed to the ASTM G-32 [43] standard recommendations, and measurements were performed by the stationary specimen method. During the test, at stated time intervals, the samples were examined by precise analytical balance weighing with accuracy of 0.01 mg. The mean depth of erosion, erosion rate and maximum erosion rate, and incubation period were estimated. Erosion stages were read from the plotted cumulative cavitation curves. The total test time lasts for 30 hours.

To identify the wear mechanism, samples were characterized before and after wear testing using X-ray diffraction (XRD), surface profilometer, atomic force microscope and SEM-EDS using BSE and topographic modes. The investigations were conducted at stated test intervals relating to samples weighting. Furthermore, the topography and surface roughness of the samples were investigated using atomic force microscope (AFM, NTE-GRA Prima (NT-MDT BV, The Netherlands) on semi-contact mode using silicon cantilever NSG30 with average resonant frequency of 300 kHz. The AFM observations were conducted at stated test time intervals: 0h, 1h and 6h. Moreover, after 30h of testing damaged areas were analysed using stick profilometer Form Talysurf Series 50mm Intra (Taylor Hobson Ltd., Lecester, England, UK). The surface roughness parameters: arithmetical mean height (S$_a$) and maximum height (S$_z$) [44,45] were determined according to the ISO 25178 standard [46]. To state the effect of the cavitation load on the microstructure, the X-ray diffraction (XRD) measurements analysis were conducted before and after CE testing. Finally, the conducted analysis allows characterizing the cavitation erosion mechanism of HiPed Stellite 6.

3. Results

3.1. Microstructure of the HIPed Stellite 6

Literature survey reports that HIPed stellites microstructure consists of cobalt-based alloy metallic matrix and second phases, mainly hard chromium carbides [47–49]. This is also confirmed by our study involving, the chemical composition analysis, metallographic and X-ray diffraction investigations which confirmed the HIPed Stellite 6. As-received K0 sample microstructure contains cobalt based solid solution matrix consisting of Co-Cr solid solution alloyed with tungsten, nickel, iron and molybdenum (**Figure 1**, spot A) as well as second-phases, carbides (**Figure 1**, spots B and C). Moreover, XRD patterns presented in **Figure 2** show that the HIPed stellite 6 matrix exhibits two crystal structures, γ (fcc – face cantered cubic) and ε (hcp – hexagonal close packed) phases. Thus, depending on whether the alloy is unimplanted or implanted these phases have different hcp to fcc ratios. **Figure 2** shows the change in XRD profile for samples implanted with nitrogen ions of two different doses compare to unimplanted sample (K0). In both cases, we can see the same and significant changes. For unimplanted sample, in XRD profile we can distinguish high intensity peaks at 2θ values of 41.18°, 44.24° and 47.03° corresponding to (100), (002) and (101) planes of hcp phase and a very weak peak at 2θ values of 51.12° from (200) planes of fcc phase. The presence of the fcc phase in the unimpeded sample is also indicated by an increase in intensity peaks at 2θ values of about 44° due to the overlap of peaks corresponding to the hcp (002) and fcc (111) planes.

While for implanted samples (K1 and K4), XRD profiles revealed a significant increase in peak's intensity at 2θ values of about 44°, 51°, 75° and 91.5°. The increase in intensity of peak at 2θ values of about 51° is directly related to the increase of fcc phase (some hcp reverts to metastable fcc). While, the increase in the intensity of the remaining peaks is related to the growth of the areas with fcc structure in the solid solution and the overlapping of the peaks from the planes: hcp (002) and fcc (111); hcp (110) and fcc (220), and hcp (212) and fcc (311), respectively (see **Figure 2**). In the case of a lower dose of ions, increase in the intensity of these peaks is greater, consequently, the hcp to fcc ratios of K1 exceeds those reported for K2. The accumulation of structural defects produced during implantation results in the absorption of energy by the material and facilitates the hcp to fcc transformation [50]. This can be clarified by recovery and removal of strain, dislocations and phase transformation hcp → fcc under implantation process (**Figure 8**). In the case of a lower dose of ions, the increase in the intensity of these three peaks is greater, which indicates that the hcp phase is first transformed to fcc phase (dose 5×10^{16} N$^+$, **Figure 2**a) and subsequently dosed until 1×10^{17} N$^+$, it is converted back to hcp phase due to absorption of higher energy (**Figure 2**b). Additionally, the ion implantation modifies the crystallite grain size, which is confirmed by broadening of the XRD diffraction peaks. From the analysis of the half-widths of the peaks for peaks that do not overlap, it can be concluded that during implantation there is a refinement of the hcp grains size from 17.9 nm (K0) to 8.8 nm and 10.4 nm for a lower and higher dose of ions, respectively. At the same time, in contrary to unimplanted sample, growth of grains with the fcc structure were observed for a lower dose of ions, with a size of 15.1 nm (K1), in comparison to grain size 11.0 nm for a higher dose of ions. Furthermore, Houdková et al [12], who studied different surface treatments of Stellite 6, confirmed that variation of hcp to fcc based phase's ratio depends on type of deposition and treatment processes. Thus, the powder metallurgy manufactured HIPed Stellite 6 phase composition differs from those reported for welded or thermally deposited stellites.
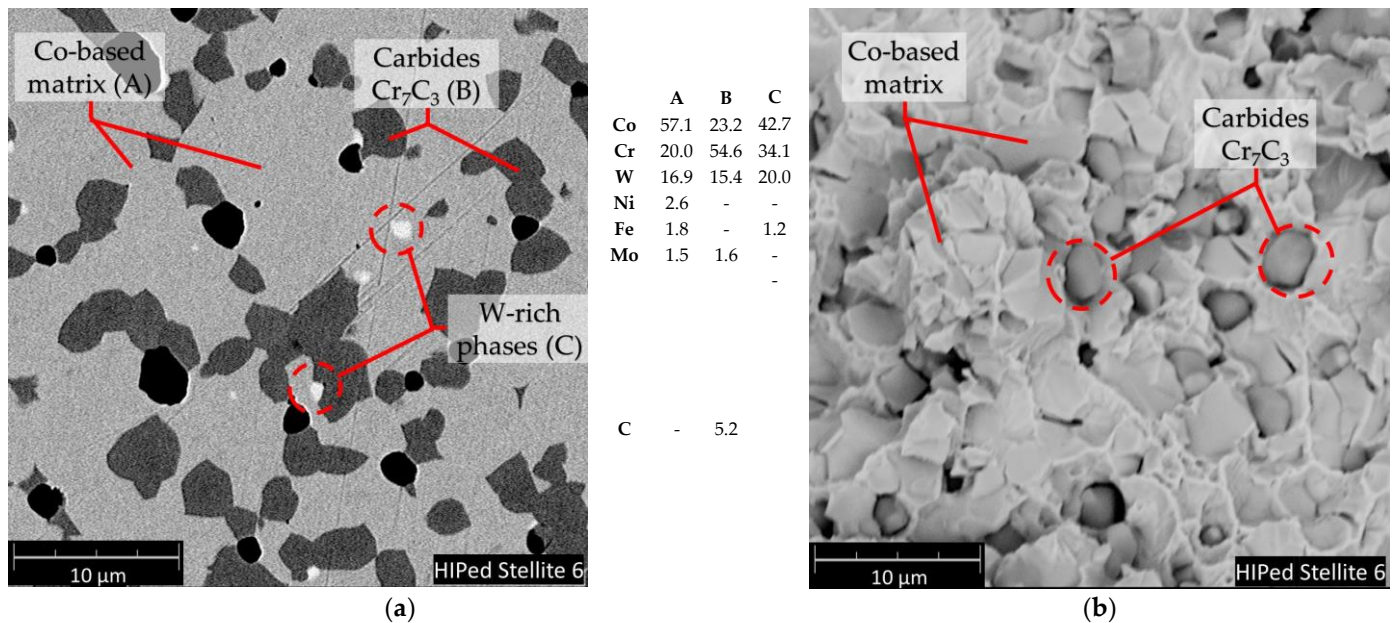
	A	B	C
Co	57.1	23.2	42.7
Cr	20.0	54.6	34.1
W	16.9	15.4	20.0
Ni	2.6	-	-
Fe	1.8	-	1.2
Mo	1.5	1.6	-
			-
C	-	5.2	

Figure 1. Microstructure of the HIPed Stellite 6 alloy: **(a)** polished top surface and chemical composition of A, B and C spots; **(b)** structure of fractured sample, SEM-EDS.
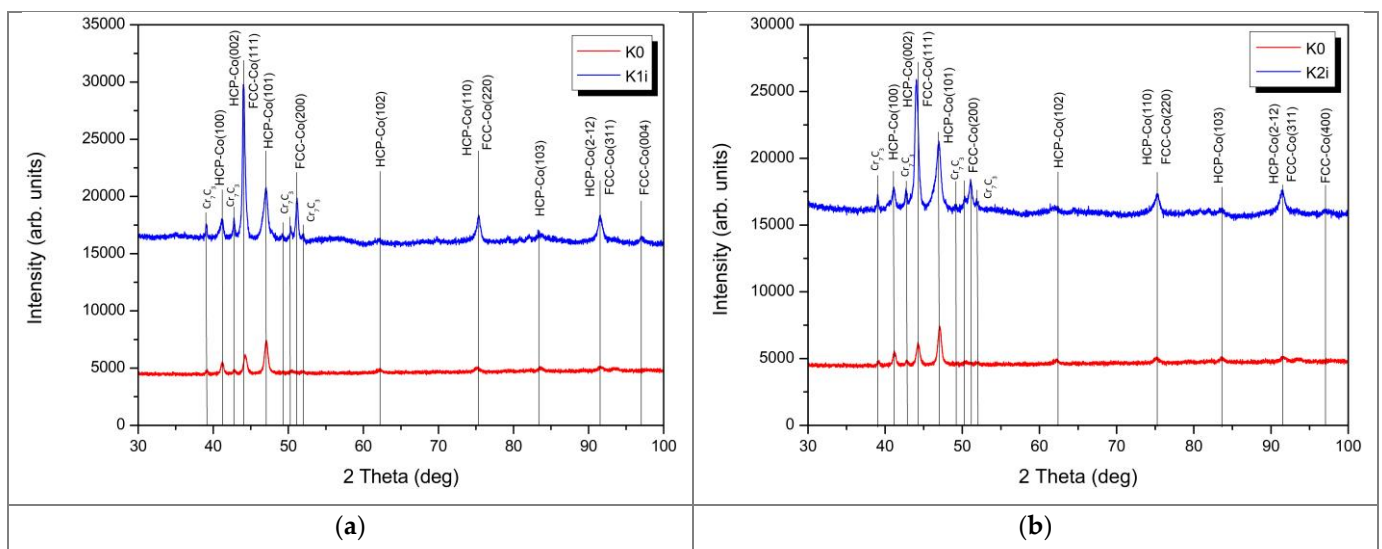

Figure 2. XRD patterns of a HIPed Stellite 6 before (red line) and after implantation (blue line) with two different doses: **(a)** 5 x 10^{16} N^+/cm^{-2} (sample K1i) **(b)** 1 x 10^{17} N^+/cm^{-2} (sample K2i).

In our work, XRD also confirms that dominant microstructure secondary phase is a chromium carbide Cr_7C_3 (indicated by the light grey areas in **Figure 1**, spot B), besides the structure contains a small amount of tungsten enriched phases (white areas, **Figure 1**, spot C). The ion implantation affects the changes of cobalt-based solid solution crystallite structure. Literature reports [51] that high-dose ion implantation of nitrogen leads to formation of nitrides. However, no nitrides were confirmed by the XRD investigation and it seems that nitrogen ion implantation results mainly in a change of hcp to fcc structure. **Figure 3** presents the distribution of implanted nitrogen ions and radiation damage (vacancies) caused by the implantation over the sample depth. It is well seen that the higher nitrogen dose results in a two-fold higher concentration of nitrogen ions, and the maximum concentration is observed at approx. 145 nm depth from the top surface while vacancies defects density is the highest at approx. 100 nm depth (**Figure 3**b). Variation of hcp to fcc phase's ratio dependence on implantation fluences. Also, the radiation defects have the maximum concentration at 100 nm depth (**Figure 3**b). On the other hand, it is reported by the literature [52,53] that the long-range effect of ion implantation could exceed the range

of nitrogen ions implanted zone. Budzyński et al [26] claimed the nitrogen ion affected zone of Stellite 6 is four times thicker than the depth of the defects, reaching about 1.0 µm thickness of the layer. This long-range effect supports the structural modification in the subsurface layer at nitrogen ion implantation and could be manifested in increase of the dislocation density [53]. To conclude, the nitrogen interaction facilitates the hcp transformation into fcc in the ion-affected subsurface zone of HIPed Stellite 6.
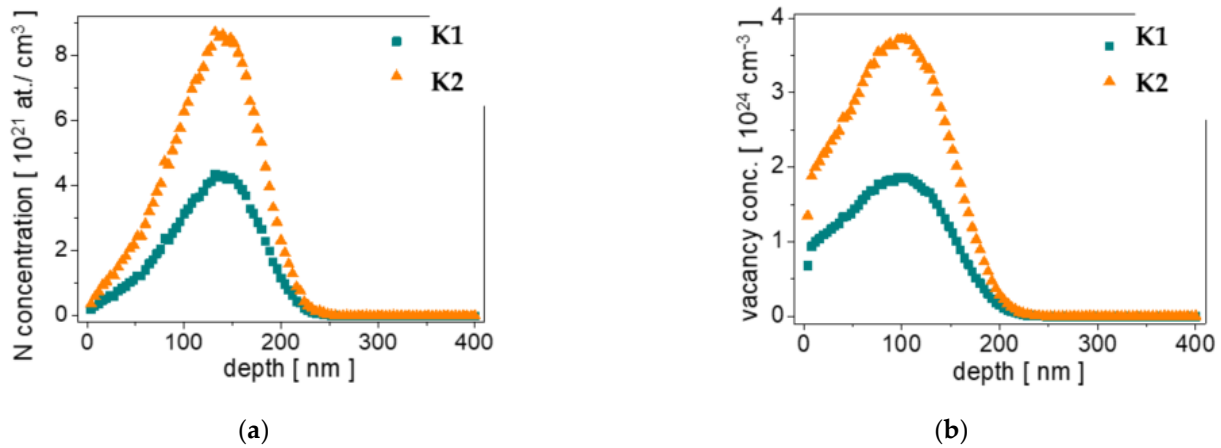
Figure 3. Theoretical distribution of implanted by 120 keV nitrogen ions with different nitrogen doses: (**a**) K1: 5×10^{16} N^{+}/cm^{-2} and K2: 1×10^{17} N^{+}/cm^{-2} (**b**); implantation-generated vacancies (radiation defects).

3.2. Cavitation erosion (CE) resistance

The cavitation erosion rate curves of unimplanted and nitrogen implanted HIPed Stellite 6 and reference stainless steel are presented in **Figure 4** while the summary of CE indicators is displayed in **Table 2**. **Figure 5** and **Figure 7** compares surface morphologies in different CE time intervals. In addition to this, the **Figure 6** displays the quantitative areal roughness S_a and S_z parameters vs time.

The nitrogen ion implantation plays an important role in controlling the CE behaviour of HIPed Stellite 6. Analysis of quantitative results confirms that the implanted HIPed Stellite 6 has almost 10 times higher resistance to CE than the stainless steel grade AISI 304. It should be noted that unimplanted stellite CE resistance is only 5-times higher than the reference AISI 304 sample. Additionally, the CE results analysis proves that the nitrogen ion implantation three times elongates the incubation period of erosion and successively mitigates the erosion rate, and decreases mass loss and mean erosion depth, see **Table 2** and **Figure 4**. Furthermore, cavitation results follow the XRD results which confirm that K1 sample presents higher fcc content and higher CE resistance than K2 sample. It should be noted that the increase of fcc structure, formed by the nitrogen ion-implantation (**Figure 2**), is essential to mitigate the erosion damage, especially in the incubation period of CE. This is supported by the analysis of surface morphology development investigated using AFM, see **Figure 5** and **Figure 6**. The unimplanted K0 microstructure is dominated by the hcp phase which has higher stacking fault energy [54] than fcc, thus it decreases the ability to work-hardening and affects matrix detachment at the carbide/solid solution interfaces. Consequently, due to cavitation loads, the surface of K0 exhibits higher roughness than implanted samples. The nitrogen-treated surfaces of samples K1 and K2 (rich in fcc) are less pronounced for deterioration and cavitation-affected surfaces are less roughened. It is known that the hcp structure has a lower ability to work hardening and is usually tougher than the fcc crystalline structure. The fcc structure is metastable at room temperature and can be transformed into hcp under strain-inducted transformation [50,55] due to cavitation. The phase transformation consumes the cavitation loads for the phase fcc → hcp and effectively decreasing the surface damage.

(**a**)   (**b**)
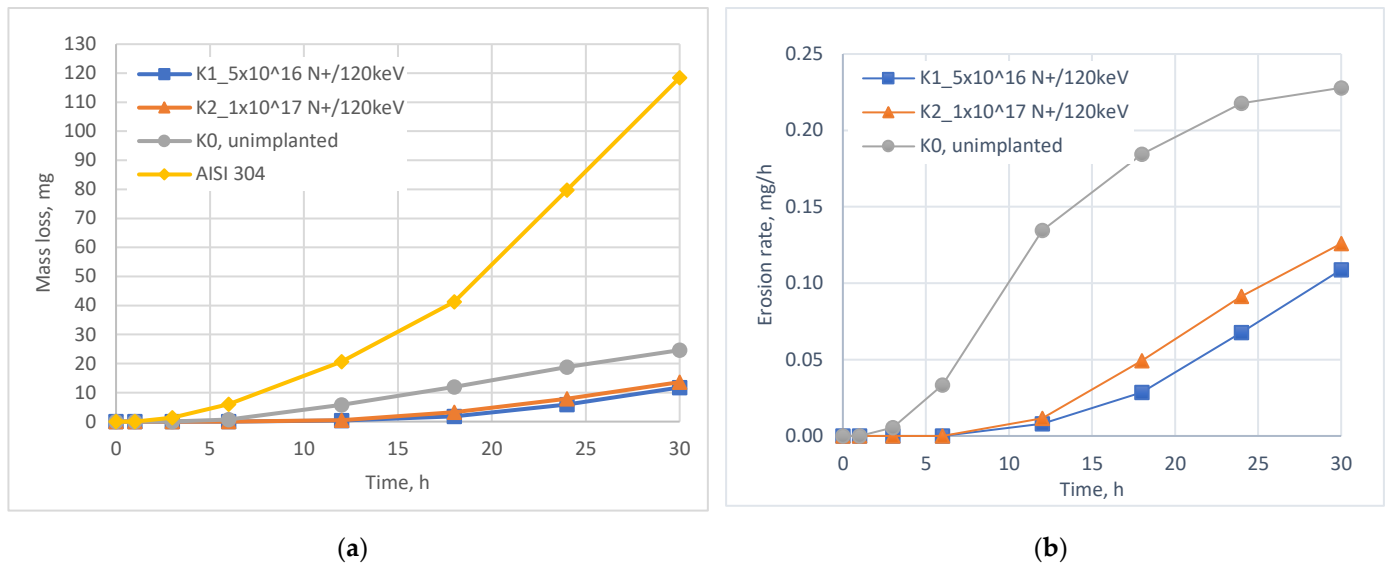
Figure 4. Cavitation erosion curves of nitrogen implanted and unimplanted HIPed Stellite 6 and reference stainless steel (AISI 304) cumulative mass loss **(a)**; **(b)** erosion rate curves of HIPed Stellite 6.

Table 2. Summary of the cavitation erosion results.

Sample	Incubation time, h	Erosion rate, mg/h	Mean erosion depth, μm
AISI 304	1.3	1.10	18.89
K0	2.0	0.23	3.69
K1	6.0	0.11	1.76
K2	6.0	0.13	2.04

Changes in the surface morphology as well as the development of S_a and S_z roughness parameters (**Figure 5**, **Figure 6** and **Figure 7**) well correlates with the CE results given in **Figure 4**. Comparable analysis of the roughness parameters during the initial stage of erosion done for the unimplanted sample K0, with nitrogen implanted samples (K1 and K2), visualised that ion treated samples display a lower rate of surface roughening, and at the end of incubation period, the K1 sample obtains the lowest roughness, **Figure 6**. This agrees with surfaces morphology visualized at stated time-exposure, for 1 and 6 hours in **Figure 5**. Besides, the 30 hours roughness of unimplanted sample K0 has higher values of S_a=1.92 μm and lower S_z=22.6 μm than estimated for nitrogen implanted K1 (S_a=1.48 μm and S_z=24.2 μm) and K2 (S_a=1.55 μm and S_z=26.9 μm). It seems that the arithmetical mean height (S_a) parameter well compares to the samples' damage rate order while the maximum height (S_z) provides information about the damage mechanism because it refers to the sum of the roughness maximum peak height and maximum valley depth. Finally, at 30 h of cavitation testing K0 presents accelerated stage of erosion and high rate of material removal than K1 and K2 samples which are in the earlier stage of CE affecting by pitting and craters formation (increasing S_z) than on uniform mode removal explained by less advanced material removal and lower mean roughness (S_a).
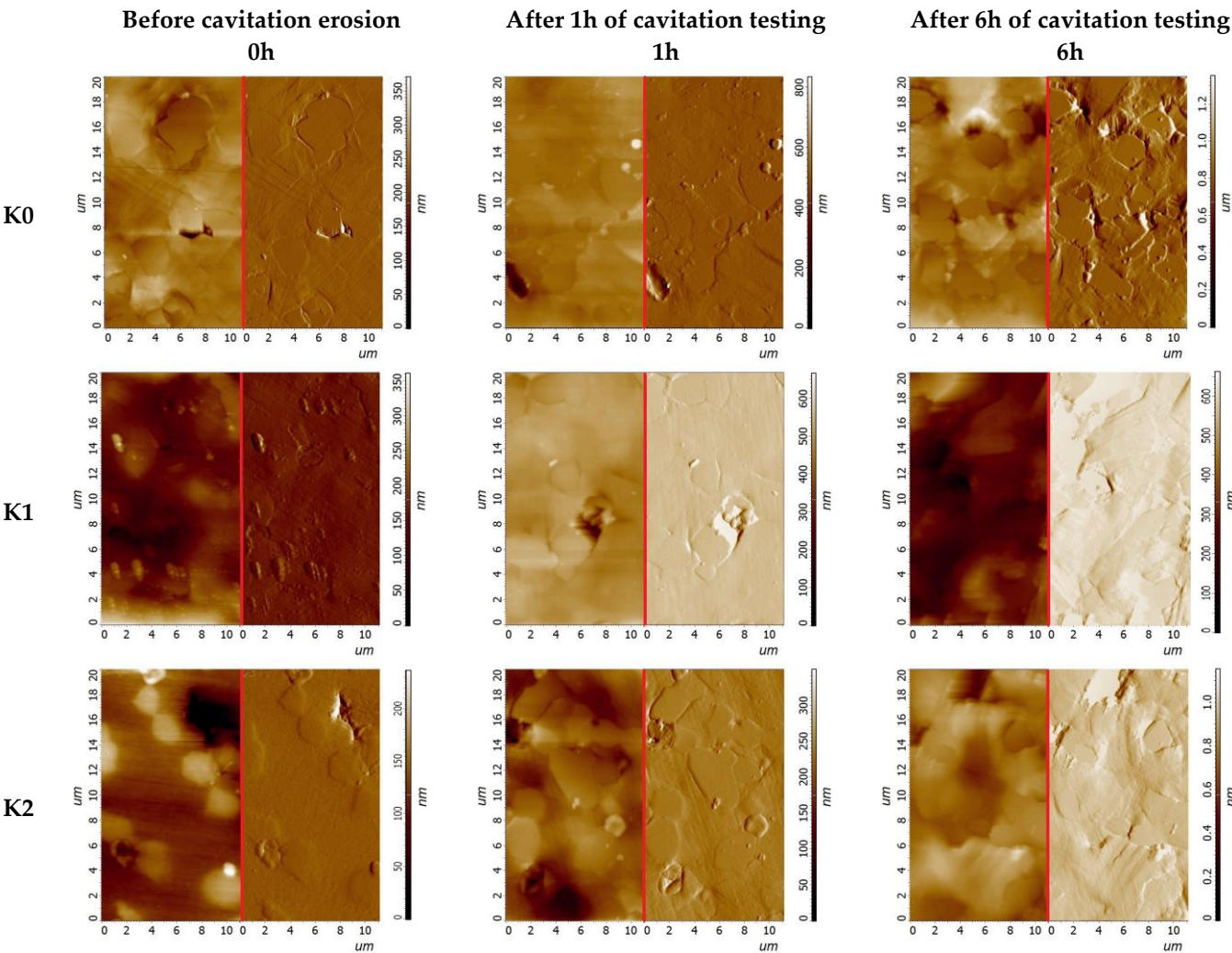
Figure 5. Surface development in initial stage of CE of HIPed Stellite 6 samples K0, K1 and K2 noted at 1 h and 6 h of cavitation testing. AFM images in high domain (left) and corresponding magnitude projection (right side of a picture).
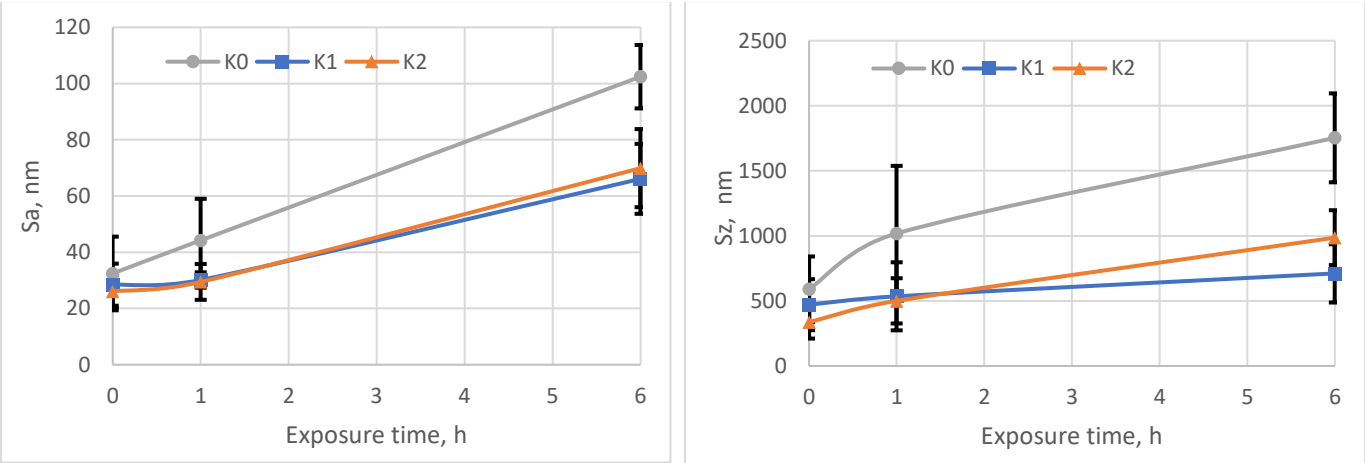

Figure 6. Areal roughness Sa and Sz parameters measured in initial stage of cavitation erosion.
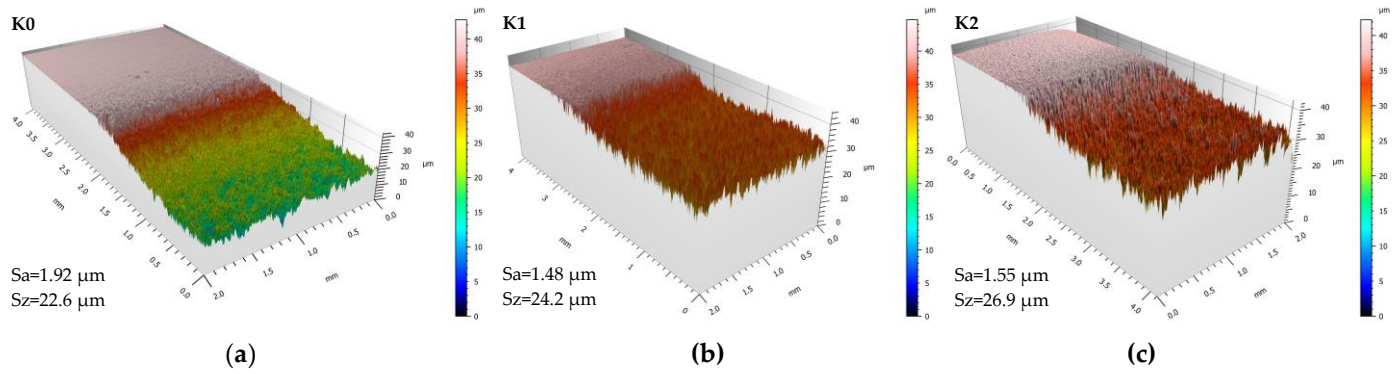
Figure 7. 3D roughness development: undamaged area and area of samples after 30 hours of cavitation testing: (**a**) unimplanted: K0-K0c; (**b**) implanted with a fluence of 5×10^{16} N$^+$/cm^2: K1-K1c; (**c**) implanted with a fluence of 1×10^{17} N$^+$/cm^2: K2-K2c.

Comparison of the cavitation effect on the X-ray profiles for unimplanted and implanted samples after 30 h of cavitation testing (labels ended with "c"; K0c, K1ic, K2ic) are presented in **Figure 8**. The XRD analysis suggests that the eroded surfaces of K1ic and K2ic (investigated after 30h) display the presence of both hcp and fcc structures, comparable to unimplanted K0 (before cavitation erosion testing). Although the proportion of the hcp to fcc for K1c and K2c differs from those identified before cavitation testing see **Figure 2**. In case of the K0c sample, it seems that the tougher and dominated by hcp surface layer of K0 poorly prevents the underneath material from degradation. In addition to this, the CE of unimplanted K0c manifests in hcp → fcc phase transformation, see **Figure 8**a. On the whole, cavitation field affecting metallic surface mainly by the mechanical action of the collapsing cavitation bubbles and microjets [56,57] which has a fatigue nature [58,59]. Additionally, a high-temperature field is also generated during cavitation [60,61] and the time-temperature effect on eroded material cannot be neglected. It is claimed by the literature that elevated temperature affects the recovery process in the crystalline structure of CoCr alloy [62]. While increasing the temperature of pure cobalt, at 417º C the hcp structure undergoes phase transformation to the high temperature fcc form [63].

The cavitation-load of implanted samples K1ic and K2ic result metastabile fcc to hcp transformation. It seems load is consumed for the strain-induced fcc → hcp martensitic transformation, see **Figure 8** (cavitation-load induces phase transformation [12]). This phenomenon is well documented in the case of unimplanted stellite alloys subjected to cavitation loads [64] and mechanical action likewise sliding wear at room and elevated temperatures [54]. Besides after 30h of the testing, in the case of K1ic and K2ic samples higher content of hcp was confirmed than for unimplanted sample K0c (indicated by lower XRD peaks intensity, see **Figure 8**). This can be explained by the proceeding martensitic transformation in the case of K1c and K2c samples and . Moreover, the effect of nitrogen ion fluences on the development of cavitated structure has been confimred. The K1c sample is much more prone to fcc formation than the K2c sample. This refers to the differences in nitrogen doses and higher fcc content after ion-implantation observed for K1 sample, see **Figure 2**. A higher nitrogen fluence reduces the cobalt based solid solution formation ability and facilitates carbides debonding, see **Figure 8**b and **8c**, as a result, ends up with the increase of CE damage of the K2 sample.

Undoubtedly, CE affects the ion-implanted HIPed Stellite 6 behaviour mainly, by elongating the incubation period of erosion and bonding the carbides in the cobalt matrix. Thus in the later period of CE the fcc structure formed due to ion implantation decreases, and the hcp phase starts to increase in K1c and K2c samples. Besides, we studied the CE behaviour until 30 h of testing when the removal of ion-modified material took place. Moreover, the martensitic transformation ability (due to fcc depletion) reduced and, severe surface roughening (see **Figure 7**) and debonding of Cr$_7$C$_3$ was initiated resulting in pit formation, see **Figure 9** and **Figure 10**). These mechanisms favour detachment of the material end exposure of deeper located hcp structures. Thus, we believed that nitrogen implanted samples in longer than 30 h exposure testing, due to the exposure of the deeper

located unimplanted bare material, should behave as K0c sample and hcp→fcc transformation is expected (as unimplanted stellite). Summing up, all these factors contribute to elongation of the incubation period, reduces the damage rate of implanted surfaces and overall positively donates for CER of nitrogen dosed HIPed Stellite 6.
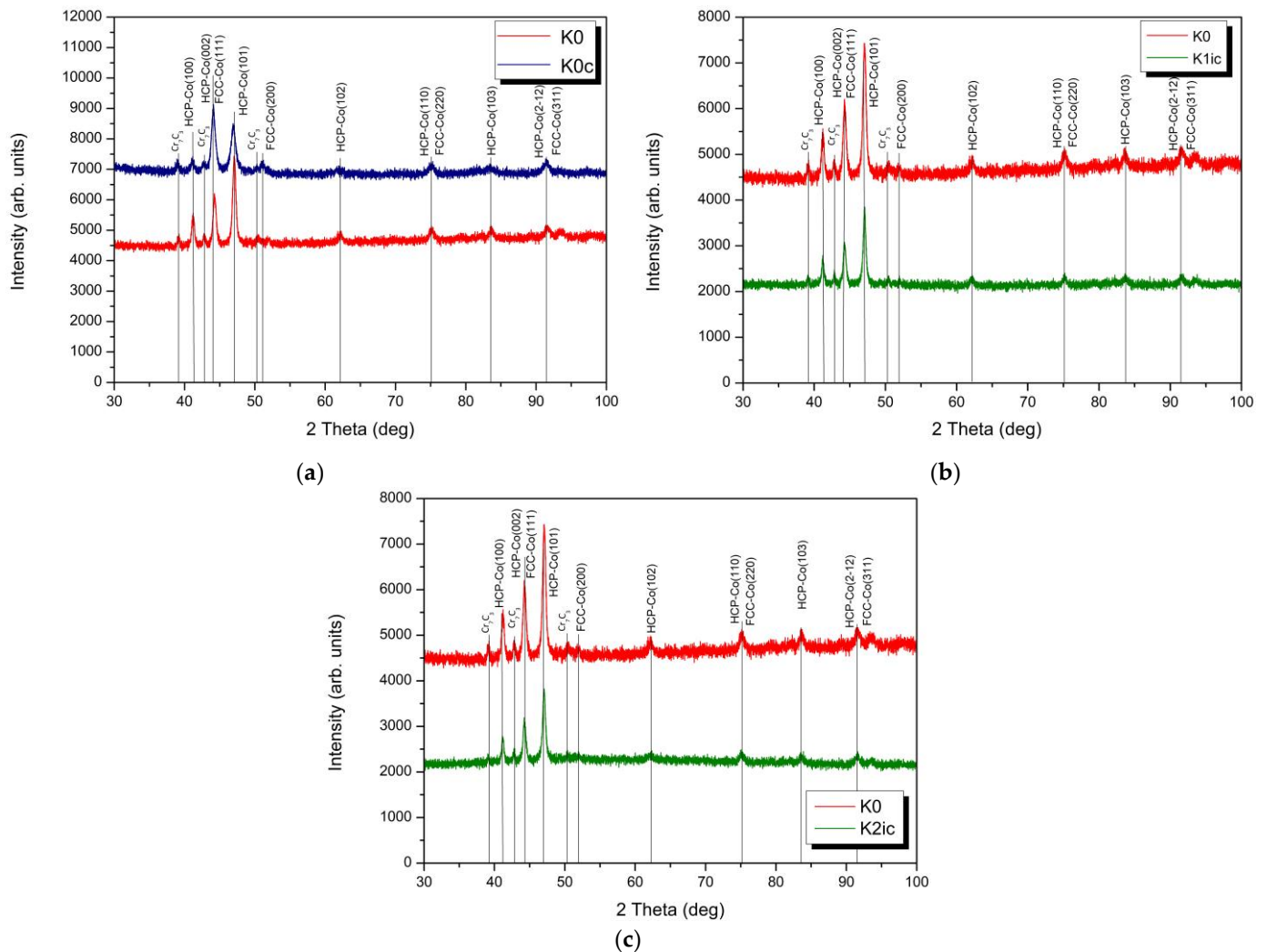

(a)

(b)

(c)

Figure 8. X-ray diffraction patterns obtained for HIPed Stellite 6 samples before and after cavitation test of: **(a)** unimplanted: **(b)** nitrogen implanted with dose of 5×10^{16} N$^+$/cm^2 (K1ic) and **(c)** nitrogen implanted with dose of 1×10^{17} N$^+$/cm^2 (K2ic).

3.3. Erosion mechanism of HIPed Stellite 6

The SEM analysis of cavitation worn surfaces (see **Figure 9** and **Figure 10**), surface morphology analyses, XRD phase investigations allows to state the erosion mechanism. Generally, the HIPed Stellite 6 initial microstructure can be simplified to two dominant phases, cobalt-based matrix and Cr_3C_7 carbides. Therefore the CE wear mechanism of HIPed stellite 6 starts at surface roughening due to plastic deformation of the cobalt-rich matrix (**Figure 5** and **Figure 6**). The cobalt-based solid solution exhibits twining but much severe deformation is observed in hcp rich phase K0 sample than for nitrogen-dosed K1 and K2 surfaces (**Figure 9** and **Figure 10**).
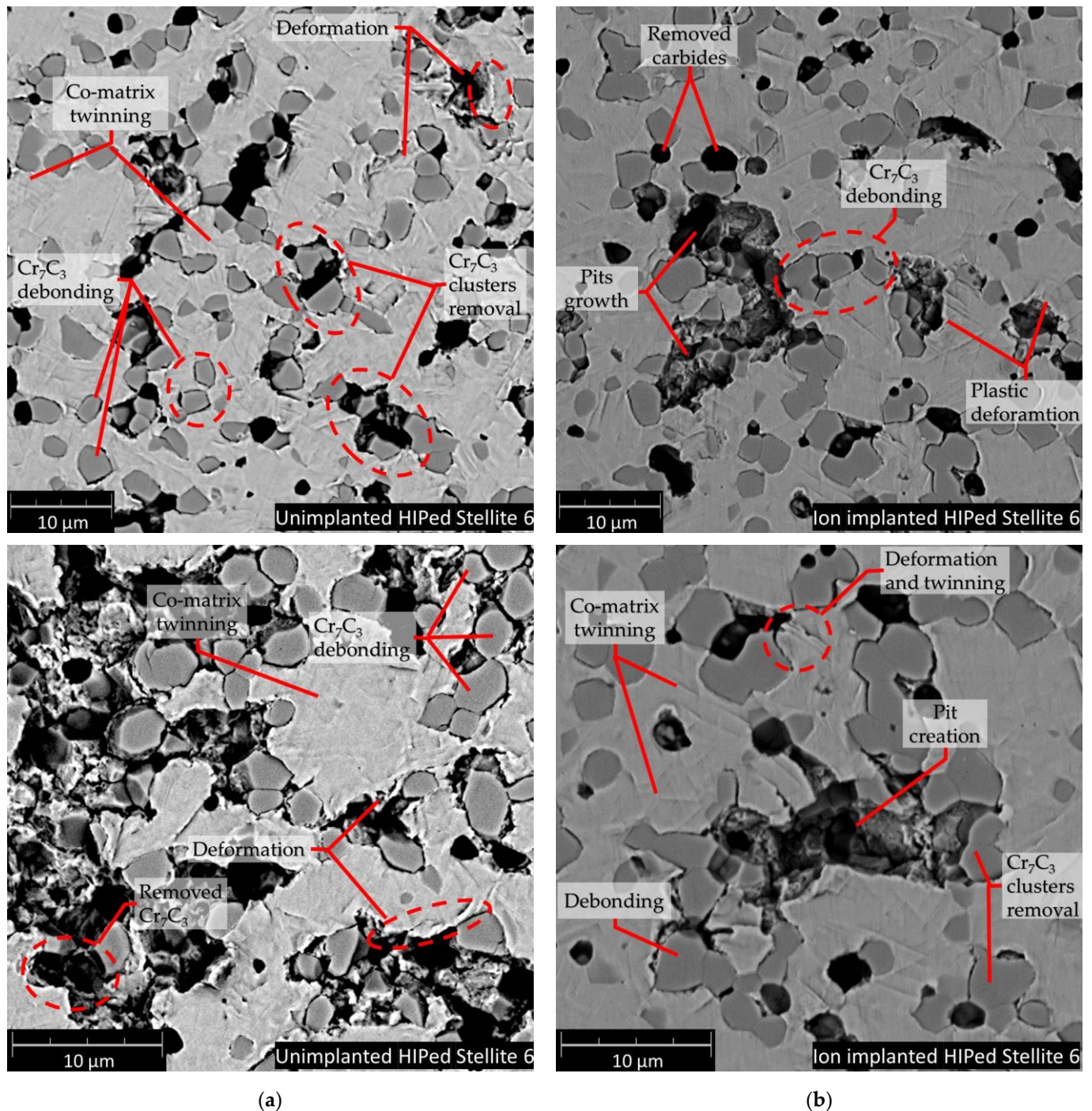
(**a**)   (**b**)

Figure 9. The initial stage of cavitation erosion of HIPed Stellite 6: (**a**) unimplanted sample (**b**) nitrogen implanted, SEM.

Twinning is a common deformation mechanism in hcp metal and alloys subjected to plastic deformation [65]. XRD investigation confirmed that nitrogen implantation of Stellite 6 provides increase of fcc crystallites, and the presence of this phase elongates the initial period of erosion, **Table 2**. The AFM areal roughness measurements confirmed (**Figure 5** and **Figure 6**) that the nitrogen implantation results in less harsh roughness development. Furthermore, fcc crystallite is prone to plastic deformation and has highier deformability than hcp and consequently prevents debonding at cobalt matrix and Cr_3C_7 interfaces (**Figure 9**). This mechanism elongates the CE incubation stage of HIPed Stellite 6. Further, deformed metallic matrix contributes to ceramic phase losses along with the ceramic clusters which firstly undergoes spallation. At the interfaces of hard carbide particles and cobalt based solid solution, the voids arose, and plastic deformation of the cobalt-austenite is present **Figure 9**. This weakens the carbide restrain and material detachment starts at the ceramic particles removal. Pits and dimples after the carbide removal

are created. Then, exposed to cavitation pit edges, which lost their support undergoes plastic deformation, and finally are also detached. The debonding and cracking in Cr_7C_3 results in spallation of the hard carbides and introduces pits which are the centre of material cracking, deformation and accelerated degradation. It should be pointed out that this damage mechanism proceeds in the lower rate for nitrogen implanted stellites, see **Figure 9**. We have noticed that the initial stage erosion behaviour of the HIPed Stellite 6 is comparable to those observed for MMC (metal matrix composites) reported in our previous study [66] for Al/Al_2O_3 and Cu/Al_2O_3 cold sprayed MMC's, mainly due to semi-metallic/ ceramic microstructure of HIPed Stellite 6 which relates to the manufacturing process (powder metallurgy). During later periods of cavitation ion affected zone is also removed (**Figure 10**). Moreover, massive material chunks are losing restarting. Erosion progresses in the deeper located unchanged/fresh structure of the material is exposed to deterioration. The cobalt matrix erosion proceeds in plastic deformation mode. The XRD analyse confirms that implanted K1 and K2 samples undergo martensitic transformation. It is expected that in further longer exposure time, in implanted samples K1 and K2 the effects of martensitic transformation comparable as for unimplanted K0 sample.

Summing up, the proposed cavitation erosion model differs from those presented for welded stellites [17] or HVOF deposited WC-CoCr cermet's [67] because this paper preliminary signalises the effect of nitrogen ion implantation on reinforcement of carbides bonding to cobalt matrix by a decrease of hcp to fcc ratio. This initial strengthen of metallic matrix reduces erosion rate due to blocking of Cr_3C_7 particles detachment and has been associated with elongation of incubation stage, consequently improving CE resistance of HIPed Stellite 6.
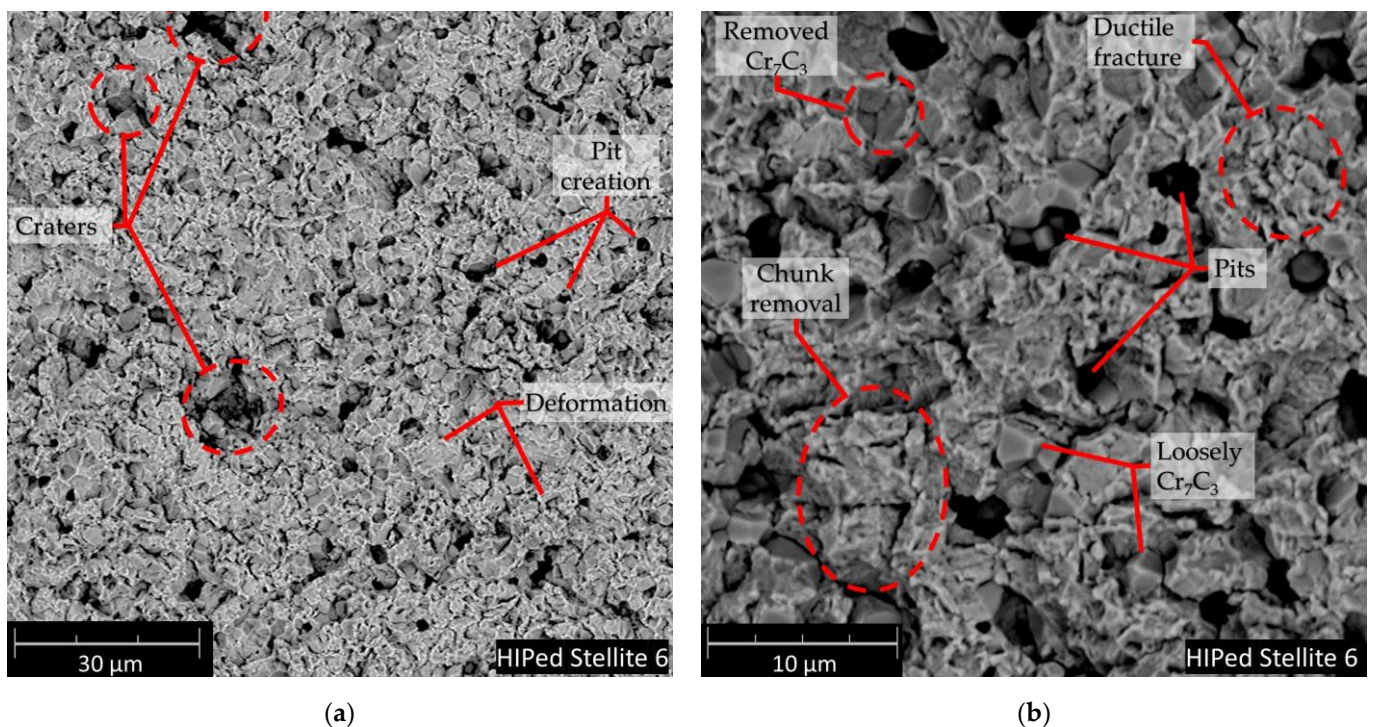

Figure 10. Damaged surface of HIPed Stellite 6 at 30 h of exposure: (**a**) surface overview (**b**) enlarged area, SEM.

5. Conclusions

This work discusses the nitrogen ion implantation effect on the cavitation erosion resistance of HIPed Stellite 6 cobalt alloy. Also, the effect of nitrogen dose was taken into account during the analysis of CE mechanism of HIPed stellite 6. Finally, the influence of cavitation on phase transformation of ion-implanted cobalt-based solid solution was preliminarily discussed. The following conclusions are drawn:

1. Ion-implanted of HIPed Stellite 6 by 120 keV with fluences 5×10^{16} N^+/cm^{-2} and 1×10^{17} N^+/cm^{-2} increases the CE resistance, finally by two times decreases the material loss, three times elongating the incubation period of erosion than for unimplanted stellite and has almost 10 times higher CE resistance than AISI 304 stainless steel.

2. The dose-effect on CE has been confirmed. Unimplanted HIPed Stellite 6 presents severe erosion due to hcp cobalt matrix decreasing the alloy deformation ability and bonding of Cr_7C_3. Nitrogen ion implantation results on $\epsilon(hcp) \rightarrow \gamma(fcc)$ transformation and fcc structure facilitates CE resistance. Stellite dosed with lower fluences of 5×10^{16} N^+/cm^{-2} has a lower hcp to fcc ratio and consequently presents increasing resistance to CE.

3. Nitrogen ion implantation of HIPed Stellite 6 strengthens the cobalt-solid solution by fcc structure formation which effectively bonds Cr_7C_3 carbides in matrix, mitigates the matrix plastic fracture, finally increasing the incubation time and decreasing erosion rate.

4. Nitrogen ion implantation initiates in hcp phase recovery process, removal of strain and dislocations and facilitates fcc phase formation. Under the cavitation-loads, nitrogen implanted HIPed Stellite 6 fcc phases well-consume the cavitation load for work-hardening and Co-based matrix martensitic fcc $\rightarrow$ hcp transformation. All those transformations beneficially contribute to decreasing the cavitation rate of implanted stellite.

5. The CE wear mechanism of HIPed Stellite 6 relies on the plastic deformation of the cobalt matrix starting at Cr_7C_3 and Co-matrix interfaces. Once the chromium carbides losing restrain, are debonding and removed. Carbides detachment creates cavitation pits which initiate cracks propagation through cobalt matrix which ends with a detachment of massive chunk of materials.

6. Undoubtedly, nitrogen ion-implantation of HIPed Stellite 6 has a beneficial effect on their CE resistance and in the future, the nitrogen ion dose and implantation energy should be optimized to form the optimal ratio of hcp to fcc in cobalt-based solid solution.

Conflicts of Interest: The authors declare no conflict of interest.

References

1. Baumann, E.; Terry, I.R. The EPR: A Clear Step Forward in Dose Reduction and Radiation Protection. *Nucl. Eng. Des.* **2006**, *236*, 1720–1727, doi:10.1016/j.nucengdes.2006.04.011.

2. Bazychowska, S.; Smoleńska, H.; Kończewicz, W. The Impact of Material Selection on Durability of Exhaust Valve Faces of a Ship Engine – A Case Study. *Adv. Sci. Technol. Res. J.* **2020**, *14*, 165–174, doi:10.12913/22998624/124074.

3. Stellite Family: Stellite Available online: https://www.stellite.com/us/en/products/stellite-family/stellite-family-stellite.html (accessed on 30 March 2021).

4. Foster, J.; Cullen, C.; Fitzpatrick, S.; Payne, G.; Hall, L.; Marashi, J. Remanufacture of Hot Forging Tools and Dies Using Laser Metal Deposition with Powder and a Hard-Facing Alloy Stellite 21®. *J. Remanufacturing* **2019**, *9*, 189–203, doi:10.1007/s13243-018-0063-9.

5. G.p., R.; M., K.; Bakshi, S.R. Hardfacing of AISI H13 Tool Steel with Stellite 21 Alloy Using Cold Metal Transfer Welding Process. *Surf. Coat. Technol.* **2017**, *326*, 63–71, doi:10.1016/j.surfcoat.2017.07.050.

6. Zhu, Z.; Ouyang, C.; Qiao, Y.; Zhou, X. Wear Characteristic of Stellite 6 Alloy Hardfacing Layer by Plasma Arc Surfacing Processes Available online: https://www.hindawi.com/journals/scanning/2017/6097486/ (accessed on 5 March 2021).

7. Liu, R.; Wu, X.J.; Kapoor, S.; Yao, M.X.; Collier, R. Effects of Temperature on the Hardness and Wear Resistance of High-Tungsten Stellite Alloys. *Metall. Mater. Trans. A* **2015**, *46*, 587–599, doi:10.1007/s11661-014-2664-8.

8. Xue, L. Chapter 16 - Laser Consolidation—A Rapid Manufacturing Process for Making Net-Shape Functional Components. In *Advances in Laser Materials Processing (Second Edition)*; Lawrence, J., Ed.; Woodhead Publishing Series in Welding and Other Joining Technologies; Woodhead Publishing, 2018; pp. 461–505 ISBN 978-0-08-101252-9.

9. Mousavi, S.E.; Naghshehkesh, N.; Amirnejad, M.; Shammakhi, H.; Sonboli, A. Wear and Corrosion Properties of Stellite-6 Coating Fabricated by HVOF on Nickel–Aluminium Bronze Substrate. *Met. Mater. Int.* **2020**, doi:10.1007/s12540-020-00697-7.

10. Lucchetta, G.; Giusti, R.; Vezzù, S.; Bariani, P.F. Investigation and Characterization of Stellite-Based Wear-Resistant Coatings Applied to Steel Moulds by Cold-Spray. *CIRP Ann.* **2015**, *64*, 535–538, doi:10.1016/j.cirp.2015.04.031.

11. Singh, R.; Kumar, D.; Mishra, S.K.; Tiwari, S.K. Laser Cladding of Stellite 6 on Stainless Steel to Enhance Solid Particle Erosion and Cavitation Resistance. *Surf. Coat. Technol.* **2014**, *251*, 87–97, doi:10.1016/j.surfcoat.2014.04.008.

12. Houdková, Š.; Pala, Z.; Smazalová, E.; Vostřák, M.; Česánek, Z. Microstructure and Sliding Wear Properties of HVOF Sprayed, Laser Remelted and Laser Clad Stellite 6 Coatings. *Surf. Coat. Technol.* **2017**, *318*, 129–141, doi:10.1016/j.surfcoat.2016.09.012.

13. Valíček, J.; Řehoř, J.; Harničárová, M.; Gombár, M.; Kušnerová, M.; Fulemová, J.; Vagaská, A. Investigation of Surface Roughness and Predictive Modelling of Machining Stellite 6. *Materials* **2019**, *12*, 2551, doi:10.3390/ma12162551.

14. Malayoglu, U.; Neville, A. Comparing the Performance of HIPed and Cast Stellite 6 Alloy in Liquid–Solid Slurries. *Wear* **2003**, *255*, 181–194, doi:10.1016/S0043-1648(03)00287-4.

15. Ratia, V.L.; Zhang, D.; Carrington, M.J.; Daure, J.L.; McCartney, D.G.; Shipway, P.H.; Stewart, D.A. The Effect of Temperature on Sliding Wear of Self-Mated HIPed Stellite 6 in a Simulated PWR Water Environment. *Wear* **2019**, *420–421*, 215–225, doi:10.1016/j.wear.2018.09.012.

16. Yu, H.; Ahmed, R.; Lovelock, H. de V.; Davies, S. Influence of Manufacturing Process and Alloying Element Content on the Tribomechanical Properties of Cobalt-Based Alloys. *J. Tribol.* **2008**, *131*, doi:10.1115/1.2991122.

17. Hattori, S.; Mikami, N. Cavitation Erosion Resistance of Stellite Alloy Weld Overlays. *Wear* **2009**, *267*, 1954–1960, doi:10.1016/j.wear.2009.05.007.

18. Díaz, V.V.; Dutra, J.C.; Buschinelli, A.J. de A.; D'Oliveira, A.S.C. Cavitation Erosion Resistance of Deposits Processed by Plasma Transferred Arc Welding. *Weld. Int.* **2009**, *23*, 159–165, doi:10.1080/09507110802543286.

19. Romo, S.A.; Santa, J.F.; Giraldo, J.E.; Toro, A. Cavitation and High-Velocity Slurry Erosion Resistance of Welded Stellite 6 Alloy. *Tribol. Int.* **2012**, *47*, 16–24, doi:10.1016/j.triboint.2011.10.003.

20. Lavigne, S.; Pougoum, F.; Savoie, S.; Martinu, L.; Klemberg-Sapieha, J.E.; Schulz, R. Cavitation Erosion Behavior of HVOF CaviTec Coatings. *Wear* **2017**, *386–387*, 90–98, doi:10.1016/j.wear.2017.06.003.

21. Ding, X.; Ke, D.; Yuan, C.; Ding, Z.; Cheng, X. Microstructure and Cavitation Erosion Resistance of HVOF Deposited WC-Co Coatings with Different Sized WC. *Coatings* **2018**, *8*, 307, doi:10.3390/coatings8090307.

22. Liu, J.; Bai, X.; Chen, T.; Yuan, C. Effects of Cobalt Content on the Microstructure, Mechanical Properties and Cavitation Erosion Resistance of HVOF Sprayed Coatings. *Coatings* **2019**, *9*, 534, doi:10.3390/coatings9090534.

23. Lamana, M.S.; Pukasiewicz, A.G.M.; Sampath, S. Influence of Cobalt Content and HVOF Deposition Process on the Cavitation Erosion Resistance of WC-Co Coatings. *Wear* **2018**, *398–399*, 209–219, doi:10.1016/j.wear.2017.12.009.

24. Shoja-Razavi, R. Laser Surface Treatment of Stellite 6 Coating Deposited by HVOF on 316L Alloy. *J. Mater. Eng. Perform.* **2016**, *25*, 2583–2595, doi:10.1007/s11665-016-2138-9.

25. Smolina, I.; Kobiela, K. Characterization of Wear and Corrosion Resistance of Stellite 6 Laser Surfaced Alloyed (LSA) with Rhenium. *Coatings* **2021**, *11*, 292, doi:10.3390/coatings11030292.

26. Budzyński, P.; Kamiński, M.; Turek, M.; Wiertel, M. Impact of Nitrogen and Manganese Ion Implantation on the Tribological Properties of Stellite 6 Alloy. *Wear* **2020**, *456–457*, 203360, doi:10.1016/j.wear.2020.203360.

27. Qin, Z.; Wu, Z.; Zen, X.; Luo, Q.; Liu, L.; Lu, W.; Hu, W. Improving Corrosion Resistance of a Nickel-Aluminum Bronze Alloy via Nickel Ion Implantation. *Corrosion* **2016**, *72*, 1269–1280, doi:10.5006/2097.

28. Morozow, D.; Barlak, M.; Werner, Z.; Pisarek, M.; Konarski, P.; Zagórski, J.; Rucki, M.; Chałko, L.; Łagodziński, M.; Narojczyk, J.; et al. Wear Resistance Improvement of Cemented Tungsten Carbide Deep-Hole Drills after Ion Implantation. *Materials* **2021**, *14*, 239, doi:10.3390/ma14020239.

29. Verma, S.; Dubey, P.; Selokar, A.W.; Dwivedi, D.K.; Chandra, R. Cavitation Erosion Behavior of Nitrogen Ion Implanted 13Cr4Ni Steel. *Trans. Indian Inst. Met.* **2017**, *70*, 957–965, doi:10.1007/s12666-016-0887-7.

30. Liu, F.; Wang, J.; Chen, D.; Xu, Y.; Zhao, M. The Cavitation Erosion of the 45# Carbon Steels Implanted with Titanium and Nitrogen. *Tribol. Trans.* **2010**, *53*, 239–243, doi:10.1080/10402000903226341.

31. Gately, N.V.H.; Dillich, S.A. Effects of Titanium Implantation on Cavitation Erosion of Cobalt-Based Metal-Carbide Systems. *Mater. Sci. Eng.* **1987**, *90*, 333–338, doi:10.1016/0025-5416(87)90229-1.

32. Turrubiates-Estrada, R.; Salinas-Rodriguez, A.; Lopez, H.F. FCC to HCP Transformation Kinetics in a Co–27Cr–5Mo–0.23C Alloy. *J. Mater. Sci.* **2011**, *46*, 254–262, doi:10.1007/s10853-010-4969-3.

33. Cabrol, E.; Boher, C.; Vidal, V.; Rézaï-Aria, F.; Touratier, F. Plastic Strain of Cobalt-Based Hardfacings under Friction Loading. *Wear* **2015**, *330–331*, 354–363, doi:10.1016/j.wear.2015.01.082.

34. Tolédano, P.; Krexner, G.; Prem, M.; Weber, H.-P.; Dmitriev, V.P. Theory of the Martensitic Transformation in Cobalt. *Phys. Rev. B* **2001**, *64*, 144104, doi:10.1103/PhysRevB.64.144104.

35. Lizárraga, R.; Pan, F.; Bergqvist, L.; Holmström, E.; Gercsi, Z.; Vitos, L. First Principles Theory of the Hcp-Fcc Phase Transition in Cobalt. *Sci. Rep.* **2017**, *7*, 3778, doi:10.1038/s41598-017-03877-5.

36. Bauer, R.; Jägle, E.A.; Baumann, W.; Mittemeijer, E.J. Kinetics of the Allotropic Hcp–Fcc Phase Transformation in Cobalt. *Philos. Mag.* **2011**, *91*, 437–457, doi:10.1080/14786435.2010.525541.

37. Turek, M.; Drozdziel, A.; Pyszniak, K.; Prucnal, S.; Maczka, D.; Yushkevich, Yu.V.; Vaganov, Yu.A. Plasma Sources of Ions of Solids. *Instrum. Exp. Tech.* **2012**, *55*, 469–481, doi:10.1134/S0020441212030062.

38. Ziegler, J.F. SRIM-2003. *Nucl. Instrum. Methods Phys. Res. Sect. B Beam Interact. Mater. At.* **2004**, *219–220*, 1027–1036, doi:10.1016/j.nimb.2004.01.208.

39. Weronika, H.; Sawa, M.; Trębicki, P.; Szala, M.; Winiarski, G. Influence of Austenitic Interlayer on the Properties of Stellite Surfacing Welds after Impact-Hardening. *Weld. Technol. Rev.* **2021**, *93*, 27–33, doi:10.26628/wtr.v93i2.1134.

40. Gomes, R.; Henke, S.; D´Oliveira, A.S. Microstructural Control of Co-Based PTA Coatings. *Mater. Res.* **2012**, *15*, 796–800, doi:10.1590/S1516-14392012005000099.

41. Łatka, L.; Michalak, M.; Szala, M.; Walczak, M.; Sokołowski, P.; Ambroziak, A. Influence of 13 Wt% TiO2 Content in Alumina-Titania Powders on Microstructure, Sliding Wear and Cavitation Erosion Resistance of APS Sprayed Coatings. *Surf. Coat. Technol.* **2021**, *410*, 126979, doi:10.1016/j.surfcoat.2021.126979.

42. Szala, M.; Łatka, L.; Awtoniuk, M.; Winnicki, M.; Michalak, M. Neural Modelling of APS Thermal Spray Process Parameters for Optimizing the Hardness, Porosity and Cavitation Erosion Resistance of Al2O3-13 Wt% TiO2 Coatings. *Processes* **2020**, *8*, 1544, doi:10.3390/pr8121544.

43. *ASTM G32-10: Standard Test Method for Cavitation Erosion Using Vibratory Apparatus*; ASTM International: West Conshohocken, Philadelphia: PA, USA, 2010;

44. Macek, W.; Branco, R.; Szala, M.; Marciniak, Z.; Ulewicz, R.; Sczygiol, N.; Kardasz, P. Profile and Areal Surface Parameters for Fatigue Fracture Characterisation. *Materials* **2020**, *13*, 3691, doi:10.3390/ma13173691.

45. Macek, W.; Branco, R.; Trembacz, J.; Costa, J.D.; Ferreira, J.A.M.; Capela, C. Effect of Multiaxial Bending-Torsion Loading on Fracture Surface Parameters in High-Strength Steels Processed by Conventional and Additive Manufacturing. *Eng. Fail. Anal.* **2020**, *118*, 104784, doi:10.1016/j.engfailanal.2020.104784.

46. 14:00-17:00 ISO 25178-2:2012 *Geometrical Product Specifications (GPS) — Surface Texture: Areal — Part 2: Terms, Definitions and Surface Texture Parameters*; 2012;

47. Kashani, H.; Laridjani, M.S.; Amadeh, A.; Khodagholi, M.; Ahmadzadeh, S. The Influence of Volumetric Dilution on the Strain Induced Γ→ε Martensitic Transformation in GTAW Processed Co–Cr–Mo Alloy. *Mater. Sci. Eng. A* **2008**, *478*, 38–42, doi:10.1016/j.msea.2007.05.061.

48. Opris, C.D.; Liu, R.; Yao, M.X.; Wu, X.J. Development of Stellite Alloy Composites with Sintering/HIPing Technique for Wear-Resistant Applications. *Mater. Des.* **2007**, *28*, 581–591, doi:10.1016/j.matdes.2005.08.004.

49. Ratia, V.L.; Zhang, D.; Carrington, M.J.; Daure, J.L.; McCartney, D.G.; Shipway, P.H.; Stewart, D.A. Comparison of the Sliding Wear Behaviour of Self-Mated HIPed Stellite 3 and Stellite 6 in a Simulated PWR Water Environment. *Wear* **2019**, *426–427*, 1222–1232, doi:10.1016/j.wear.2019.01.116.

50. Sort, J.; Nogués, J.; Suriñach, S.; Baró, M.D. Microstructural Aspects of the Hcp-Fcc Allotropic Phase Transformation Induced in Cobalt by Ball Milling. *Philos. Mag.* **2003**, *83*, 439–455, doi:10.1080/0141861021000047159.

51. SOUKIEH*, M. Structural-Phase Changes in Al6061-T6 Alloy during High-Dose N2 + Implantation. *Radiat. Eff. Defects Solids* **2004**, *159*, 73–79, doi:10.1080/10420150310001654043.

52. Budzynski, P. Long-Range Effect in Nitrogen Ion-Implanted AISI 316L Stainless Steel. *Nucl. Instrum. Methods Phys. Res. Sect. B Beam Interact. Mater. At.* **2015**, *342*, 1–6, doi:10.1016/j.nimb.2014.09.004.

53. Sharkeev, Yu.P.; Kozlov, E.V. The Long-Range Effect in Ion Implanted Metallic Materials: Dislocation Structures, Properties, Stresses, Mechanisms. *Surf. Coat. Technol.* **2002**, *158–159*, 219–224, doi:10.1016/S0257-8972(02)00212-8.

54. Kashani, H.; Amadeh, A.; Ohadizadeh, A. Effect of Temperature on the Strain Induced Γ→ε Phase Transformation in Stellite 21 during Wear Test. *Mater. Sci. Eng. A* **2006**, *435–436*, 474–477, doi:10.1016/j.msea.2006.07.022.

55. Meng, Q.; Guo, S.; Zhao, X.; Veintemillas-Verdaguer, S. Bulk Metastable Cobalt in Fcc Crystal Structure. *J. Alloys Compd.* **2013**, *580*, 187–190, doi:10.1016/j.jallcom.2013.05.115.

56. Huang, W.H.; Chen, K.C.; He, J.L. A Study on the Cavitation Resistance of Ion-Nitrided Steel. *Wear* **2002**, *252*, 459–466, doi:10.1016/S0043-1648(01)00897-3.

57. Li, Z.X.; Zhang, L.M.; Ma, A.L.; Hu, J.X.; Zhang, S.; Daniel, E.F.; Zheng, Y.G. Comparative Study on the Cavitation Erosion Behavior of Two Different Rolling Surfaces on 304 Stainless Steel. *Tribol. Int.* **2021**, *159*, 106994, doi:10.1016/j.triboint.2021.106994.

58. Krella, A.K.; Krupa, A. Effect of Cavitation Intensity on Degradation of X6CrNiTi18-10 Stainless Steel. *Wear* **2018**, *408–409*, 180–189, doi:10.1016/j.wear.2018.05.015.

59. Steller, J. Cavitation Damage as a Result of Polyfractional Erosion Process. *Wear* **2020**, *456–457*, 203369, doi:10.1016/j.wear.2020.203369.

60. Merouani, S.; Hamdaoui, O.; Rezgui, Y.; Guemini, M. Theoretical Estimation of the Temperature and Pressure within Collapsing Acoustical Bubbles. *Ultrason. Sonochem.* **2014**, *21*, 53–59, doi:10.1016/j.ultsonch.2013.05.008.

61. Ashokkumar, M. The Characterization of Acoustic Cavitation Bubbles – An Overview. *Ultrason. Sonochem.* **2011**, *18*, 864–872, doi:10.1016/j.ultsonch.2010.11.016.

62. Marques, F.P.; Scandian, C.; Bozzi, A.C.; Fukumasu, N.K.; Tschiptschin, A.P. Formation of a Nanocrystalline Recrystallized Layer during Microabrasive Wear of a Cobalt-Chromium Based Alloy (Co-30Cr-19Fe). *Tribol. Int.* **2017**, *116*, 105–112, doi:10.1016/j.triboint.2017.07.006.

63. Liu, R.; Yao, M.X.; Patnaik, P.C.; Wu, X. Effects of Heat Treatment on Mechanical and Tribological Properties of Cobalt-Base Tribaloy Alloys. *J. Mater. Eng. Perform.* **2005**, *14*, 634–640, doi:10.1361/105994905X64567.

64. Xiaojun, Z.; Procopiak, L.A.J.; Souza, N.C.; d'Oliveira, A.S.C.M. Phase Transformation during Cavitation Erosion of a Co Stainless Steel. *Mater. Sci. Eng. A* **2003**, *358*, 199–204, doi:10.1016/S0921-5093(03)00297-1.

65. Zhang, X.Y.; Li, B.; Tu, J.; Sun, Q.; Liu, Q. Non-Classical Twinning Behavior in Dynamically Deformed Cobalt. *Mater. Res. Lett.* **2015**, *3*, 142–148, doi:10.1080/21663831.2015.1034297.

66. Szala, M.; Łatka, L.; Walczak, M.; Winnicki, M. Comparative Study on the Cavitation Erosion and Sliding Wear of Cold-Sprayed Al/Al2O3 and Cu/Al2O3 Coatings, and Stainless Steel, Aluminium Alloy, Copper and Brass. *Metals* **2020**, *10*, 856, doi:10.3390/met10070856.

67. Taillon, G.; Pougoum, F.; Lavigne, S.; Ton-That, L.; Schulz, R.; Bousser, E.; Savoie, S.; Martinu, L.; Klemberg-Sapieha, J.-E. Cavitation Erosion Mechanisms in Stainless Steels and in Composite Metal–Ceramic HVOF Coatings. *Wear* **2016**, *364–365*, 201–210, doi:10.1016/j.wear.2016.07.015.